The observational evidence that all microflares that accelerate electrons to high-energies are rooted in sunspots

Andrea Francesco Battaglia[1,2,3], Säm Krucker[2,4], Astrid M. Veronig[5,6], Muriel Zoë Stiefel[2,3], Alexandar Warmuth[7], Arnold O. Benz[2,3], Daniel F. Ryan[2], Hannah Collier[2,3], and Louise Harra[3,8]

[1] Istituto ricerche solari Aldo e Cele Daccò (IRSOL), Faculty of informatics, Università della Svizzera italiana, Locarno, Switzerland
e-mail: `andrea.francesco.battaglia@irsol.usi.ch`
[2] University of Applied Sciences and Arts Northwestern Switzerland (FHNW), Bahnhofstrasse 6, 5210 Windisch, Switzerland
[3] Institute for Particle Physics and Astrophysics (IPA), Swiss Federal Institute of Technology in Zurich (ETHZ), Wolfgang-Pauli-Strasse 27, 8039 Zurich, Switzerland
[4] Space Sciences Laboratory, University of California, 7 Gauss Way, 94720 Berkeley, USA
[5] Institute of Physics, University of Graz, Universitätsplatz 5, A-8010 Graz, Austria
[6] Kanzelhöhe Observatory for Solar and Environmental Research, University of Graz, Kanzelhöhe 19, 9521 Treffen, Austria
[7] Leibniz-Institut für Astrophysik Potsdam (AIP), An der Sternwarte 16, D-14482 Potsdam, Germany
[8] Physikalisch-Meteorologisches Observatorium Davos, World Radiation Center, 7260 Davos Dorf, Switzerland

ABSTRACT

Context. In general, large solar flares are more efficient at accelerating high-energy electrons than microflares. Nonetheless, we sometimes observe microflares that accelerate electrons to high energies. Their origin is unclear.
Aims. We statistically characterize microflares with strikingly hard spectra in the hard X-ray (HXR) range, which means that they are efficient in accelerating high-energy electrons. We refer to these events as "hard microflares."
Methods. We selected 39 hard microflares, based on their spectral hardness estimated from the Solar Orbiter/STIX HXR quicklook light curves in two energy bands. The statistical analysis is built upon spectral and imaging information from STIX, combined with EUV and magnetic field maps from SDO/AIA and SDO/HMI.
Results. The key observational result is that all hard microflares in this dataset have one of the footpoints rooted directly within a sunspot (either in the umbra or the penumbra). This clearly indicates that the underlying magnetic flux densities are large. For the events with the classic two-footpoints morphology, the absolute value of the mean line-of-sight magnetic flux density (and vector magnetic field strength) at the footpoint rooted within the sunspot ranges from 600 to 1800 G (1500 to 2500 G), whereas the outer footpoint measures from 10 to 200 G (100 to 400 G), therefore about 10 times weaker. In addition, approximately 78% of hard microflares, which exhibited two HXR footpoints, have similar or even stronger HXR flux from the footpoint rooted within the sunspot. This contradicts the magnetic mirroring scenario. The median footpoint separation, measured through HXR observations, is approximately 24 Mm, which aligns with regular events of similar GOES classes. In addition, about 74% of the events could be approximated by a single loop geometry, demonstrating that hard microflares typically have a relatively simple morphology. Out of these events, around 54% exhibit a relatively flat flare loop geometry.
Conclusions. We conclude that all hard microflares are rooted in sunspots, which implies that the magnetic field strength plays a key role in efficiently accelerating high-energy electrons, with hard HXR spectra associated with strong fields. This key result will allow us to further constrain our understanding of the electron acceleration mechanisms in flares and space plasmas.

Key words. Sun: corona – Sun: flares – Sunspots – Sun: X-rays, gamma rays

1. Introduction

To understand the physics underpinning solar flares, it is crucial to understand how particles are accelerated to high energies. These accelerated particles carry a significant amount of the total flare energy (e.g., Hudson & Ryan 1995).

In the context of solar flares, three primary particle acceleration mechanisms have been reported in the literature (Aschwanden 2004): DC electric field acceleration (e.g., Holman 1985; Drake et al. 2006), stochastic acceleration (e.g., Stix 1992), and shock acceleration (e.g., Ellison & Ramaty 1985). Electric field acceleration, proposes the acceleration within quasi-steady electric fields, which can be produced in current sheets, during magnetic reconnection events, or within current-carrying loops. Stochastic acceleration mechanisms revolve around ran-

dom energy gains and losses in a turbulent plasma (Aschwanden 2004). Shock acceleration mechanisms involve an inhomogeneous shock front that is suitable to transfer momentum and energy to intercepted particles (Aschwanden 2004).

Regardless of the specific mechanism, particles are accelerated in the corona. These accelerated particles either move outward along "open" field lines to escape to interplanetary space or downward along closed field lines towards the denser chromosphere, where they emit radiation across the entire electromagnetic spectrum, including hard X-rays (HXRs). Although HXRs account for only a small fraction of the total radiated energy, they can serve as a useful diagnostic tool, inferring the energy of the accelerated particles deposited in the chromosphere (Fletcher et al. 2011; Benz 2017). In this study, we focus in the energy

range from 4 to 150 keV, which are photons mainly produced by electrons.

The accelerated electrons moving downward deposit their energy into the chromosphere and lower transition region, heating the plasma to high temperatures observable in the soft X-ray (SXR) range (Benz 2017). This heated plasma then follows the flare loop, extending into the corona via a process known as "chromospheric evaporation" (e.g., Hirayama 1974; Antonucci et al. 1984; Fisher et al. 1985; Veronig et al. 2002). The observable correlation between the SXR flux originating from the heated plasma and the cumulative HXR flux from the accelerated electrons is known as the Neupert effect (Neupert 1968).

Evaporation can be categorized into two types: explosive (e.g., Milligan et al. 2006a) and gentle (e.g., Milligan et al. 2006b). These categories are distinguished by the speed at which the chromospheric plasma, once heated, expands into the corona. Studies indicate that the velocity of this expansion depends upon the intensity of the accelerated electron beam that reaches the chromospheric plasma (e.g., Fisher et al. 1985). Moreover, the electron spectrum plays a crucial role, with low-energy electrons proving more effective in heating the atmosphere (which subsequently triggers evaporation) compared to their high-energy counterparts (Reep et al. 2015).

The amount of chromospheric evaporation is related to the plasma heating and the emitted SXR flux. This SXR emission is a defining factor in differentiating a (standard) flare from a microflare[1]. Microflares are dynamic, small-scale energy release events, with several orders of magnitude smaller energy regular flares. Despite their relatively smaller scale, microflares exhibit intriguing characteristics. For instance, standard (or regular) microflares are known for their steep (or soft) HXR spectra, which suggests that they are less efficient at accelerating high-energy electrons compared to larger flares (e.g., Battaglia et al. 2005; Hannah et al. 2008a, 2011; Inglis & Christe 2014; Warmuth & Mann 2016b). However, there are microflare observations of remarkably hard spectra (e.g., Hannah et al. 2008b; Ishikawa et al. 2013; Lysenko et al. 2018; Battaglia et al. 2023; Saqri et al. 2024), which implies the presence of prominent nonthermal emission due to high energy electrons. This indicates that factors other than the flare energy significantly influence the acceleration efficiency. Investigating such factors would allow us to further constrain the acceleration mechanism in flares.

In a recent case study of two microflares with hard spectra, Saqri et al. (2024) found that both events have one of their footpoints directly rooted within the sunspots (either in the umbra or the penumbra), suggesting that the strong magnetic field of the sunspot may be responsible for the hard microflare spectrum. From observations taken by the Spectrometer/Telescope for Imaging X-rays (STIX; Krucker et al. 2020), the X-ray telescope on board the Solar Orbiter mission (Müller et al. 2020), we collected 39 microflares characterized by hard HXR spectra, which we call "hard microflares." The location of the footpoints in relation to the associated sunspot was determined.

Section 2 details the data analysis. The results are presented in Sect. 3. In Sect. 4 we discuss our findings. Finally, our conclusions are drawn in Sect. 5.

2. Event selection and data analysis

In this section we describe the data analysis of STIX, AIA and HMI observations. In our analysis, we examined 39 hard mi-

---

[1] We refer to Appendix A for the description of what we consider to be a microflare.

croflares, as detailed in Table A.1. The selection method for these microflares is described in Appendix A.

2.1. STIX data analysis

In order to study the X-ray signal of the selected hard microflares, we use the observations by STIX, the X-ray telescope aboard Solar Orbiter. Due to the varying distance between the Solar Orbiter spacecraft and the Sun compared to the Earth, there is a difference in the photon arrival time. To account for this difference, all time measurements made by STIX have been adjusted and are expressed in Earth UT.

As hard microflares tend to have a relatively short high-energy burst (tens of seconds to a few minutes), as shown in Fig. 1, we use the STIX quicklook data for event selection (see Appendix A). This data product aids automatic detection for two reasons: firstly, this data is continuously accessible at a 4 s cadence, unlike spectrogram or pixel data where the integration time changes throughout each flare, and secondly, the same energy bands are consistently available.

The STIX ground-software (version 0.5.2, as of March 2024) was used for the preparation of the STIX data.

2.1.1. X-ray spectroscopy

For the spectral fitting of the STIX observations, spectrogram data have been used. The spectral fitting has been performed using the Object Spectral Executive (OSPEX; Schwartz et al. 2002) software available through the SolarSoftWare (SSW; Freeland & Handy 1998).

In this work, all spectral parameters were derived from fitting the STIX spectra around the time of the peak at high energies. The integration time around this peak is typically 10 to 20 seconds, depending on the counting statistics.

In Fig. 2, we present four different STIX spectra along with the fits as examples. To obtain the background-subtracted spectra, we only subtracted the STIX observations taken during quiet times, closest to the flare events. This is because, during quiet times, the signal is dominated by the onboard calibration source. The low-energy part of the spectrum was fitted with a standard isothermal model (the `vth` function in OSPEX). Here, we used coronal abundances, with the default set in the CHIANTI database version 10.0.1 (Dere et al. 1997; Del Zanna & Young 2020).

Due to the nature of the high-energy peaks, which are impulsive, relatively short and decrease rapidly, they have been interpreted as nonthermal emission originating from accelerated electrons injected into the chromosphere. This interpretation is also supported by X-ray and ultraviolet (UV) images (Sect. 3). Therefore, to fit the high-energy part of the spectrum, we used the standard thick-target model `thick2_vnorm` function available in OSPEX. For this fitting, we considered only a single power-law, and the resulting low-energy cutoff is always around 10 to 20 keV.

2.1.2. X-ray imaging

In the reconstruction of the STIX images, similar to the spectroscopy analysis, we considered times around the nonthermal peak (i.e., the high-energy peak). Given that the events discussed in this paper exhibit hard spectra, and that the STIX background between 10 to 20 keV is the lowest, which corresponds also to the energy range where microflares typically exhibit nonthermal
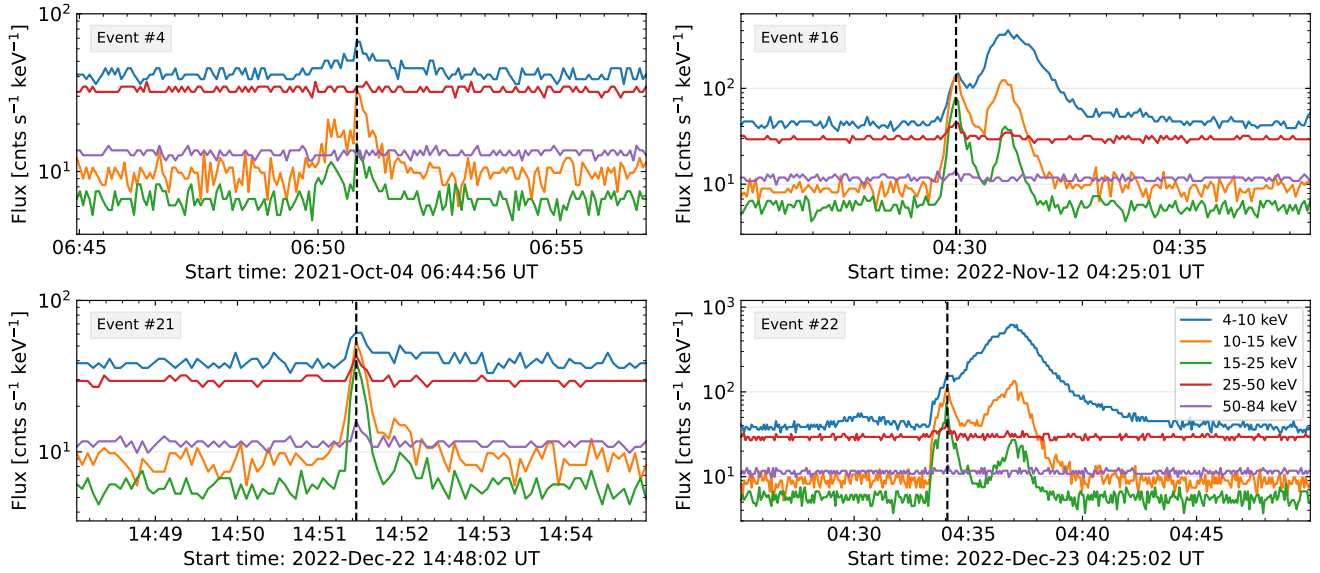
Fig. 1. STIX quicklook time profiles of four representative hard microflares from our sample. The energy range of the different curves is indicated in the legend located in the bottom right panel. The background-subtracted GOES classes for these events are A2 (event #4), B4 (event #16), A8 (event #21), and C1 (event #22), respectively. The vertical black dashed line represents the nonthermal peak time.
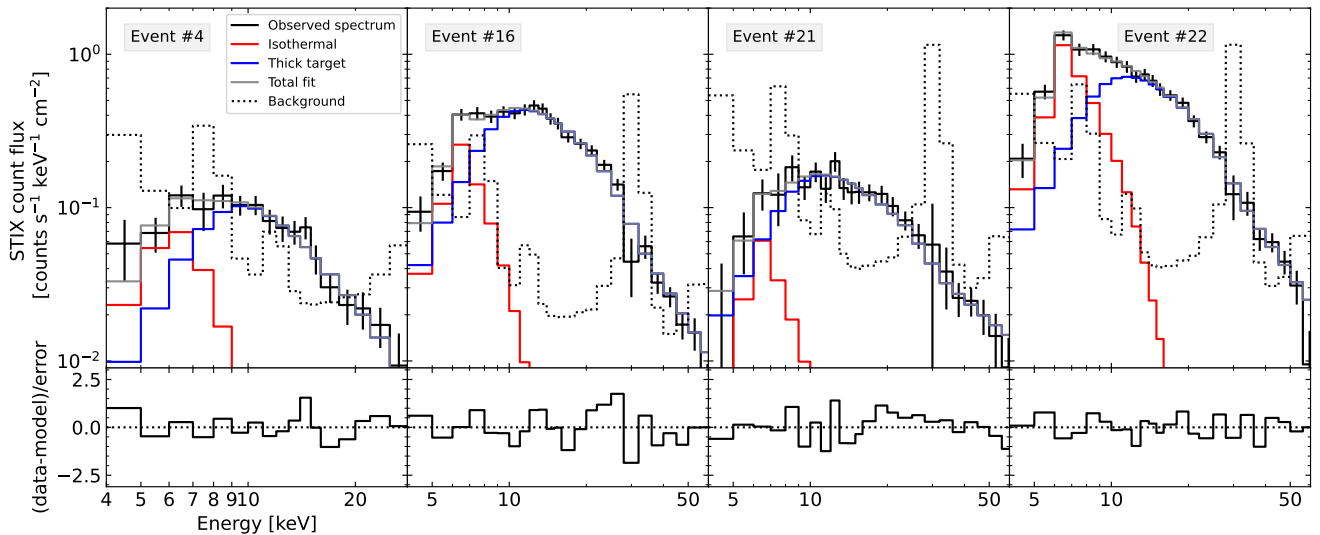

Fig. 2. STIX spectra for the same events shown in Fig. 1. The solid black line illustrates the observed, background-subtracted flare spectra, while the dashed black lines display the background. The thermal and nonthermal models are represented by the red and blue curves, respectively. The sum of the two models is shown as a gray line. Beneath each spectrum, the residuals are provided, which are calculated by subtracting the total fit from the data and normalizing the result by the error bar.

emission, this allows for easier nonthermal image reconstruction compared to thermal images. This is not typically the case, since for standard microflares, if imaging reconstruction can be done, this is mostly in the thermal range. An illustrative example is the second event from the left in Fig. 2. Here, we have a high count rate to use for nonthermal image reconstruction, whereas the thermal component is below the background rate. In such a case, it is not possible to obtain reliable image reconstructions of the thermal microflare emission. When this situation occurs, we considered times around the thermal peak for obtaining a thermal image. However, for many events, the thermal and nonthermal peak roughly coincide, making it impossible to obtain a reliable thermal image. In this paper, we considered 39 events (refer to

Sect. A): Thermal images could be obtained from 28 events and nonthermal images from almost all events, 34 in total.

The CLEAN algorithm (Högbom 1974) has been used to reconstruct all images, using natural weighting. The size of the selected CLEAN beam corresponds to the angular resolution of the sub-collimators associated with grid label 3 (Krucker et al. 2020), which is 14.6 arcsec. The sub-collimators associated with the finest grids, labeled 1 and 2, were excluded from the analysis as their calibration is still in progress.

For image co-alignment, the nonthermal images were aligned with the UV sources observed in the AIA 1600 Å maps, which typically show the flare ribbons. More details are provided in the following subsection.

To estimate the X-ray flux coming from each nonthermal source, we used the STIX visibility forward-fit algorithm (Volpara et al. 2022). We assumed that the sources were circular Gaussians, as they tend to be compact sources in hard microflares, particularly when located within the sunspots. The location of each source was then fixed, based on the locations obtained from the previously generated CLEAN image. Consequently, while the location was kept fixed, both the sizes of the sources and their respective fluxes were allowed to vary.

2.2. AIA and HMI data analysis

The data from the Atmospheric Imaging Assembly (AIA; Lemen et al. 2012) and the Helioseismic and Magnetic Imager (HMI; Scherrer et al. 2012), instruments aboard the Solar Dynamics Observatory (SDO; Pesnell et al. 2012), were obtained from the Joint Science Operations Center (JSOC). The AIA maps were calibrated using the aiapy software (Barnes et al. 2020). Visualizations, including images, histograms, spectra, scatter plots, and time profiles, were generated using SunPy (SunPy Community et al. 2020).

To overlay the STIX reconstructed images on top of the AIA maps, we first reprojected the AIA 1600 Å images to match the Solar Orbiter vantage point using the standard tools provided by SunPy. We then co-aligned the STIX images with the reprojected maps, by aligning the nonthermal sources to align with the flare ribbons that can be observed in the UV maps.

In order to estimate the photospheric magnetic field density at the footpoints of the flare loops, we used the line-of-sight magnetic field data from the HMI magnetograms (in Appendix B, we used vector magnetic field data). We obtained the flux density by averaging over the flare ribbon area, as defined by the AIA 1600 Å images. The uncertainties on the magnetic field density derives from the standard deviation within the same flare ribbon area. For this part of the analysis, we only considered events located within 50 deg longitude from the disk center as seen from Earth, which are 27 events in total.

3. Results

3.1. Visible, UV, EUV, and HXR images

Since all the STIX events discussed in this paper were also observed from Earth view, we compared the location of the flare ribbons with the location of the source active regions and sunspots using SDO imaging in the UV and visible. Afterwards, we investigated the flare morphology by comparing the AIA and HMI observations with the STIX images.

3.1.1. Footpoint locations

Before examining the location of all hard microflares, we focused on one active region, AR12882. Our aim was to compare the location of different types of flares, such as "standard" microflares (those with softer spectra or even no nonthermal emission), hard microflares, and relatively large flares. Figure 3 displays some events that occurred within AR12882 from October 4th, 2021, to October 10th, 2021. This figure clearly shows that hard microflares are rooted directly in sunspots, whereas standard microflares are located away from the sunspots in the plage regions surrounding the AR. This is in agreement with what is reported in Saqri et al. (2024). Larger flares, like the M2 class flare in Fig. 3, are more spatially extended and eventually cross sunspot areas during their time evolution. This is already known

and reported in the literature (e.g., Maurya et al. 2012; Kleint et al. 2016).

The novelty here is that all hard microflares are rooted in sunspots. This is not only true for the events from AR12882 but for all events listed in Tab. A.1.

It should be noted, however, that in some cases, part of one of the ribbons seem to be located at the edge of the penumbra, as it is the case of the event 20 in Fig. 4. For this reason, we introduced a category for distinguishing them from the events clearly rooted in sunspots. However, the fact that they appear to be at the edge of the sunspot, may be due to the inclination of the magnetic field lines, especially in the penumbra, as the location of the flare footpoints have been deduced from chromospheric altitudes. Therefore, an inclined magnetic field line in the photosphere, may result in a location at the edge of the sunspot if observed at chromospheric altitudes. What is clear, is that the standard microflares are way more distant from sunspots than the hard microflares at the edge of sunspots. The standard microflares can be 50 arcsec away or more from the sunspots, while the hard microflares are within or at the edge. This indicates that they are still magnetically connected to the sunspot. It should be noted that the selection criteria of hard microflares impacts the number of detected events categorized as at the edge of sunspots (see Appendix A.2).

3.1.2. Flare loop geometry

Figure 5 presents the AIA 131 Å images of six hard microflare events. These images show the heated flare loop. To analyze their geometry, we overlaid two reference loops on top of the AIA images. One represents a standard semi-circle loop geometry (solid orange), and the other represents a flat geometry (dashed orange), which we defined as a semi-ellipse with its semi-minor axis being half of the semi-major axis. For these examples, events 5 and 6 appear to be flat loops. Both events originated from the same AR and similar location, suggesting a similar magnetic field morphology during their occurrence. Event 10 also seems to be a flat loop. This is not the case for events 13, 22, and 32. Event 22, however, seems to show a high degree of tilting.

This type of analysis has been performed for all events in our sample (with the exception of event 12, as there is no AIA coverage) and their corresponding flare loop geometry can be found in the last column of Tab. A.1. If we could not determine whether a loop was flat or a semi-circle proxy, we labeled it either as 'unclear' when it was difficult to distinguish between these two categories (for instance, during events close to the disk center), or as 'complex' when the loop geometry could not be approximated by a single loop, or as 'tilted' when a significant degree of tilting was required.

About 74% (28 out of 38) of the events could be approximated by a simple loop geometry, demonstrating that hard microflares typically have a relatively simple geometry. Of these 28 events, it was not possible to distinguish between a semi-circle or flat loop geometry in 4 cases due to their orientation or location relative to the disk center. For the remaining 24 events, 13 (54%) displayed a flat geometry, 8 (33%) had a semi-circle geometry, and 3 required a high degree of tilting.

We note that projection effects may influence these results, as the representation of loops on a 2D image can be modified by changing the tilt or height of the loop. Therefore, to help the investigation of the loop geometry, magnetic field extrapolations could be beneficial.
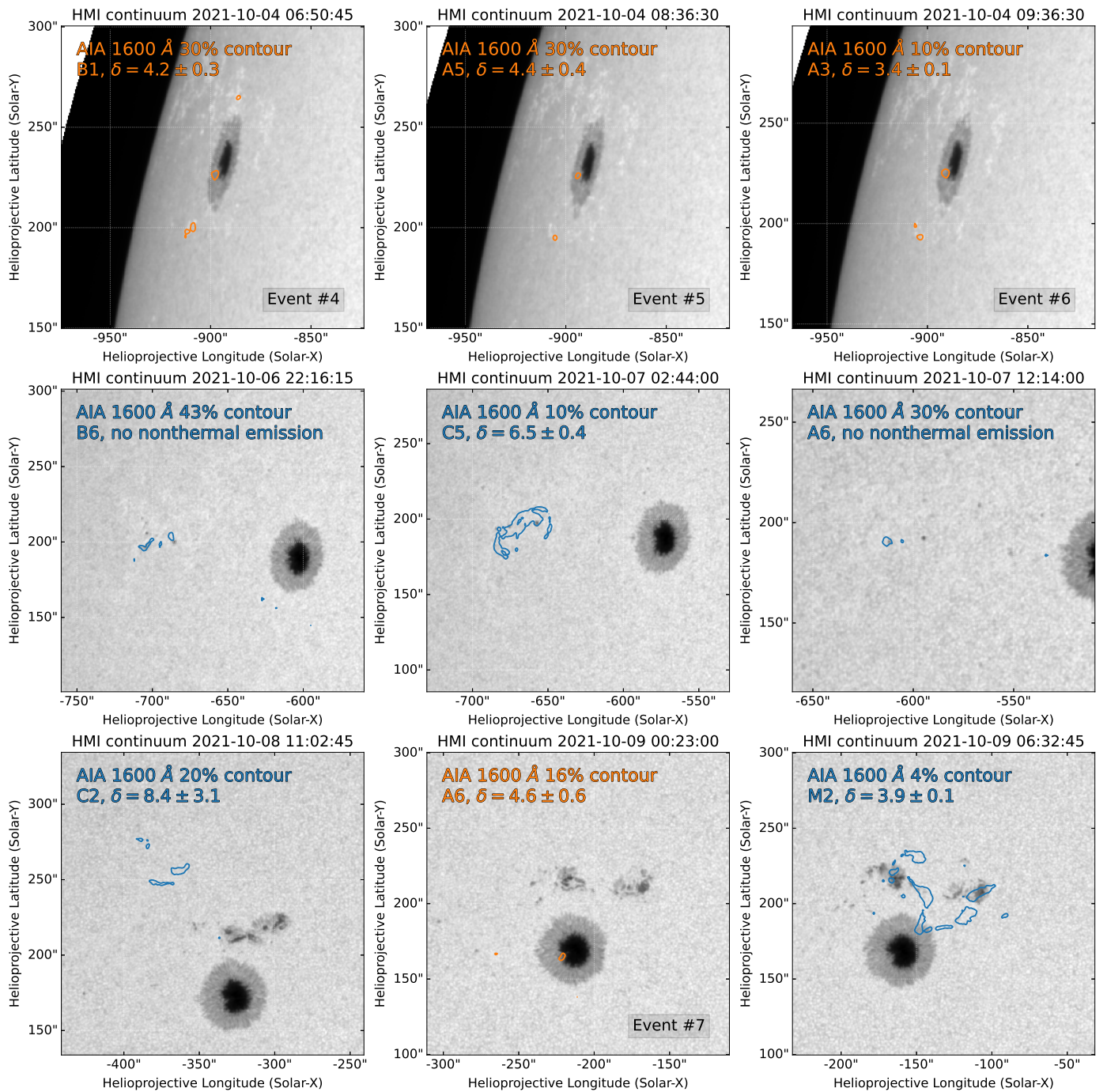
Fig. 3. Flare ribbon location of various types of flares (standard microflares, hard microflares, and a medium-size flare) that occurred within AR12882. The orange contours represent the flare ribbons identified in the AIA 1600 Å images of the hard microflares, while the blue contours represent all other events. The intensity map from SDO/HMI is plotted in the background. The legend includes the percentage of the AIA 1600 Å contour used, the GOES class, and the electron spectral index δ. This figure clearly shows that hard microflares are rooted in sunspots (umbra or penumbra), while standard microflares, which have a soft spectrum or a total lack of nonthermal emission, are located far from sunspots.

3.2. HXR spectral parameters

We are now interested in comparing the electron spectral index and the photon flux derived from the thick target model of hard microflares with previous studies.

The left panel of Fig. 6 displays the electron spectral index against the background-subtracted GOES 1-8 Å flux for different flares. This plot reveals several remarkable features. First of all, the correlation curve by Warmuth & Mann (2016a), derived from flare observations of GOES classes larger than C1, aligns well with the independent studies involving microflares (GOES A and B class events) as reported in Hannah et al. (2008a) and Battaglia et al. (2005). This correlation suggests that the flare SXR intensity correlates with the hardness of its spectrum, which turns out to be true for both flare and microflare regimes. Secondly, previous studies on microflares with relatively hard spectra (Saqri et al. 2024; Awasthi et al. 2024; Battaglia et al. 2023; Lysenko et al. 2018; Ishikawa et al. 2013; Hannah et al. 2008b) align
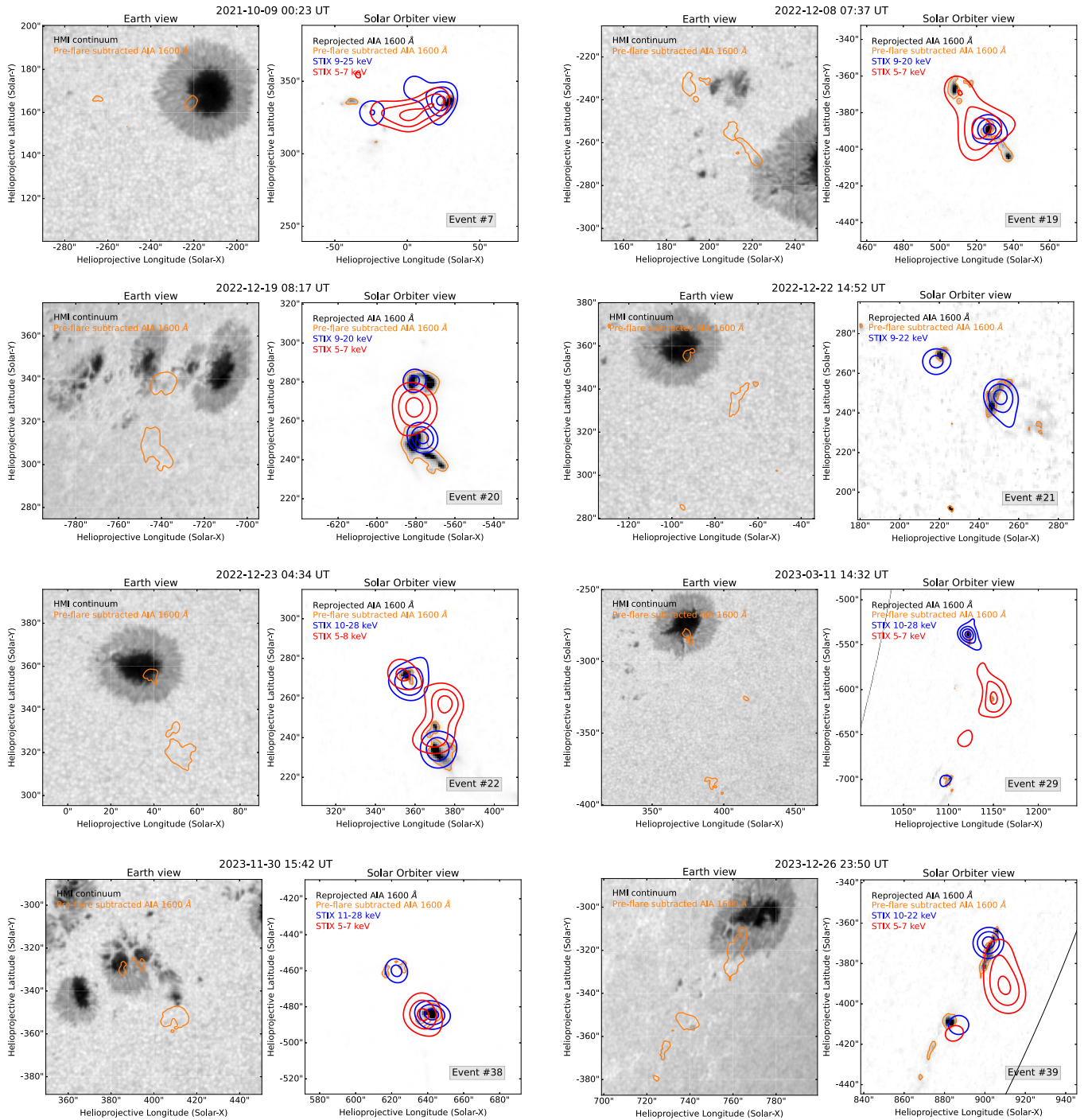
Fig. 4. Solar Orbiter/STIX HXR images of eight hard microflares. For each event, the left panel displays the SDO/HMI intensitygram and the pre-flare subtracted SDO/AIA 1600 Å contours (orange) from the Earth's perspective. The right panel shows the SDO/AIA 1600 Å image closer to the nonthermal peak time reprojected to the Solar Orbiter view, with orange the reprojected pre-flare subtracted SDO/AIA 1600 Å contours. The STIX images are displayed as red (thermal emission) and blue (nonthermal emission) contours. The event number is displayed in the bottom-right corner.

well with the hard microflares analyzed in this paper[2]. Therefore, in the discussion section, we will consider the main findings of these previous studies to infer characteristics from these events.

It is remarkable to note that some of these events are as hard as X-class flares, despite being of GOES A or B class.

The right panel of Fig. 6 shows the photon flux at 35 keV in comparison to the background-subtracted GOES 1-8 Å flux. The correlation curve deduced by Battaglia et al. (2005) aligns with the RHESSI microflare statistics by Hannah et al. (2008a). This plot reveals that hard microflares, including the event re-
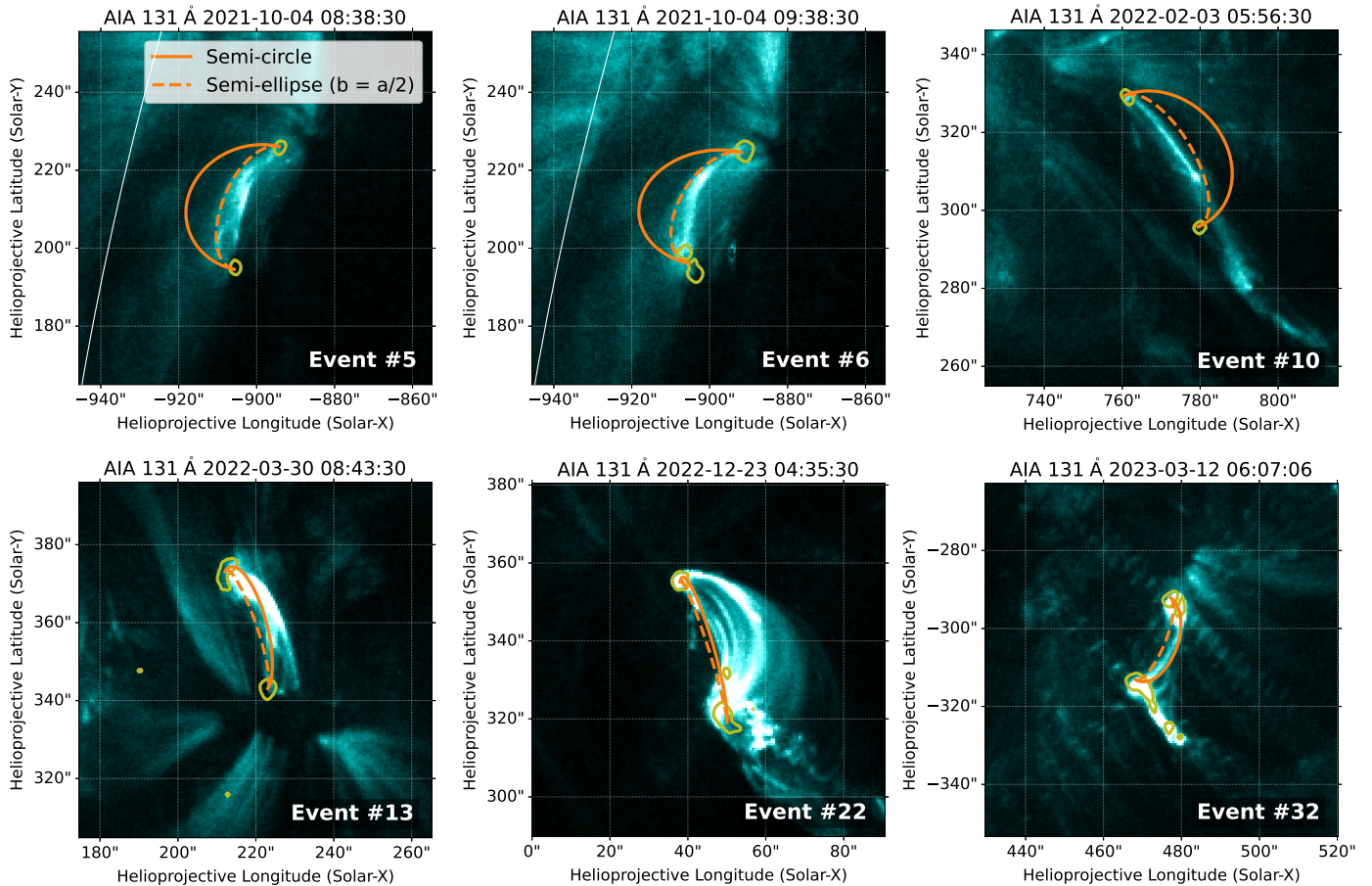
_____

[2] It is important to note that the GOES flux values presented in Fig. 6 for the events discussed by Lysenko et al. (2018) differ from those reported in their original paper. This difference arises from a different definition of the background-subtracted GOES flux.

Fig. 5. Heated flare loops of six hard microflares with SDO/AIA 131 Å images. Overlaid on the AIA 131 Å images are reference loops: a solid orange semi-circle perpendicular to the solar surface, with a radius defined as half the distance between the UV ribbons (AIA 1600 Å, green contours), and a dashed orange semi-ellipse, where its semi-minor axis is half of the semi-major one. The latter is considered a reference for flat loops.

ported in Hannah et al. (2008b), present a larger photon flux at 35 keV compared to typical events with similar SXR fluxes. Generally, hard microflares have 10 to 100 times more photon flux at 35 keV than the standard microflares of similar intensities. This suggests that an A class hard microflare typically has the photon flux at 35 keV of a standard B or C class flare.

3.3. HXR footpoint fluxes and distances

Since the reconstruction of the nonthermal footpoints of hard microflares works relatively well, we now examine their HXR fluxes and separation in the context of the classic two-footpoints flare geometry.

Figure 7 shows the histogram of the HXR flux coming from the footpoint above the sunspot relative to the total flux of the two HXR sources, for the events with two HXR sources. Among all the events with two footpoints, 59.3% display a stronger HXR flux in the footpoint rooted within the sunspot. Conversely, 18.5% have similar fluxes (within one sigma of the average relative error on the fluxes given by the forward fit algorithm), and another 22.2% show a stronger HXR flux in the footpoint outside the sunspot. In addition to the events with two footpoints, there are seven events with a single HXR footpoint. By co-aligning the location of this footpoint and the corresponding thermal source with EUV and UV images, it turns out that all seven events are correlated with the ribbon in the sunspot. Therefore, for hard mi-

croflares, there is a tendency to have a stronger HXR flux at the footpoint rooted in the sunspot. This behavior is actually inconsistent with the expectations of electron motion and magnetic mirroring in simple magnetic loops. This issue will be discussed in more detail in Sect. 4.4.

In addition to their fluxes, we estimated the distances of the two HXR sources. We show the results in Fig. 8. Most events have a separation between 15 to 30 Mm, with a median distance of about 24 Mm. These values align with Saint-Hilaire et al. (2008) for events of similar duration.

In Sect. 3.1.2, we reported that approximately 74% of the flare loops of hard microflares could be represented using a single loop geometry. About one-third of them fit a semi-circle, while half with a flat loop (i.e., a semi-ellipse, where the semi-minor axis is half of the semi-major one). Therefore, we can estimate the loop-height using the separation between the footpoints. With a median separation of about 24 Mm, the loop-height would be 12 Mm for a semi-circle geometry and 6 Mm for a flat geometry. These estimates are consistent with the values found in Christe et al. (2011). Hence, the loop-height of hard microflares is similar to those of standard microflares.

In order to determine if there is a systematic transport effect on the electrons generating the observed HXR nonthermal flux coming from the flare footpoints, we studied the total HXR count flux from the flare footpoints versus the footpooint separation. However, no correlation between these quantities is found, sug-
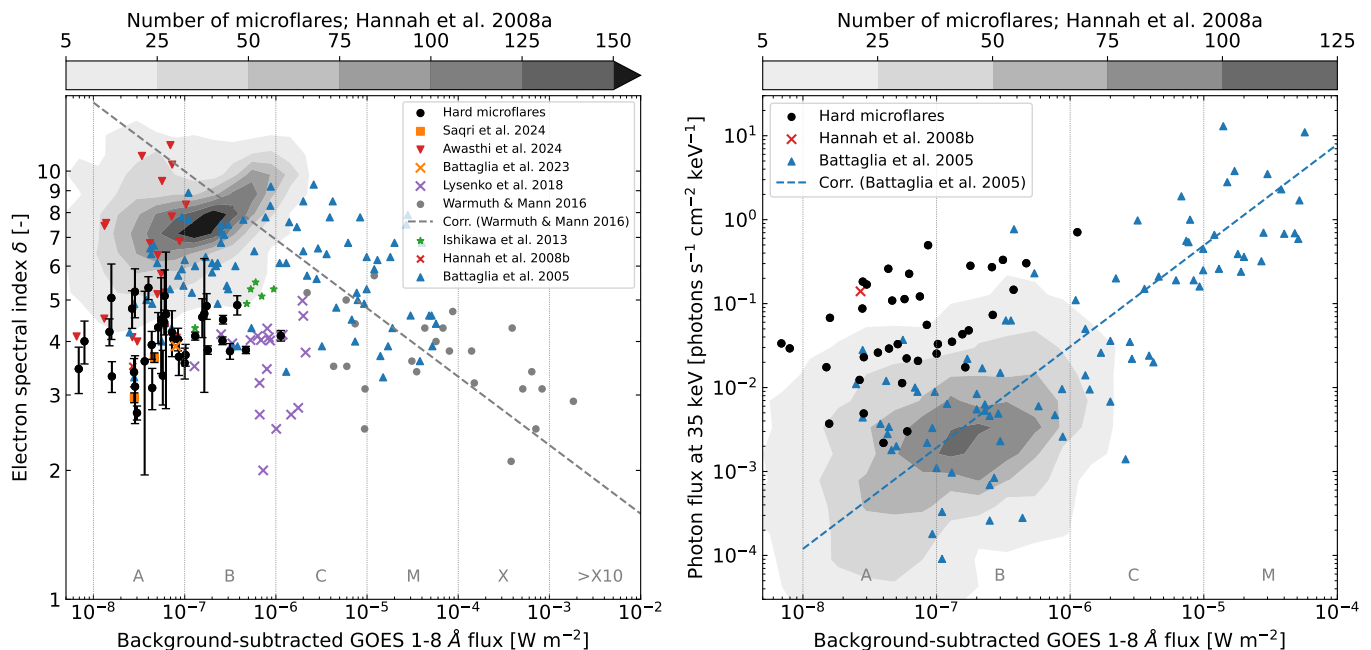
Fig. 6. Comparison of the HXR spectral parameters of the hard microflares with events reported in the literature. (*Left*) Electron spectral index δ as a function of the background subtracted GOES 1-8 Å SXR flux. Black circles represent the hard microflares considered in this paper. As a reference, we report studies of general flare and microflare samples (Warmuth & Mann 2016a; Hannah et al. 2008a; Battaglia et al. 2005), and studies which included microflares with hard spectra (Saqri et al. 2024; Awasthi et al. 2024; Battaglia et al. 2023; Lysenko et al. 2018; Ishikawa et al. 2013; Hannah et al. 2008b). These studies are detailed in the legend. The gray contour levels correspond to the RHESSI microflare study by Hannah et al. (2008a). The gray dashed line represents the correlation curve deduced by Warmuth & Mann (2016a) from the observations of flares above the GOES C1 level. (*Right*) HXR photon flux at 35 keV plotted against the background subtracted GOES 1-8 Å SXR flux. Black dots represent the hard microflares. The blue triangles and the blue dashed curve are taken from Battaglia et al. (2005), while the red cross is from Hannah et al. (2008b). The gray contour levels again refer to the RHESSI microflare study by Hannah et al. (2008a).

gesting that we cannot infer any potential transport effect of the electrons through the loop due to the varying length they have to travel within the loop. Other factors play a more significant role in determining the flux at the footpoints.

3.4. Line-of-sight magnetic field density

Given the discovery that hard microflares are directly rooted in sunspots (umbra or penumbra), we investigate the strength of the magnetic field at the flare footpoints.

The left panel of Fig. 9 displays the average photospheric line-of-sight (LoS) magnetic flux density of the footpoint within the sunspot against the electron spectral index. There is a slight tendency for events within sunspots to be harder, indicated by the mean value (dashed vertical lines). This difference, however, is within the standard deviation, suggesting that a larger sample of events might provide a clearer picture. However, it is notable that events with the strongest magnetic field (> 1500 G) are among the hardest, while those with a weaker field (< 600 G) tend to show a softer spectrum.

Because the penumbral fields are typically close to horizontal, in Appendix B we performed a similar analysis as presented in the left panel of Fig. 9, but, instead of using the HMI magnetogram data, we used the HMI vector magnetic field data (see Fig. B.1). The results are in agreement with the left panel of Fig. 9, with two relevant differences. First of all, the overall field strength is more elevated, because the vector magnetic field data consider the total field strength and not only the line-of-sight component. Secondly, there is a larger sample of harder events,

with respect to Fig. 9, to be associated with stronger magnetic field strengths (> 2000 G). This reflects the true nature of the strong magnetic fields in sunspots, regardless of the magnetic field orientation with respect to the line-of-sight as it is the case for the standard magnetograms.

The right panel of Fig. 9 compares the magnetic flux density (multiplied by $1/\cos(u)$, with u the angular distance from disk center of the flare location) to the background-subtracted GOES 1-8 Å flux. When the flux densities associated with the hard microflares are compared to flares of various classes reported in Tschernitz et al. (2018), it becomes clear that the magnetic field is much stronger for the hard microflares. By extrapolating the expected field density from the correlation curve reported in Tschernitz et al. (2018, Figure 9), GOES A and B class flares should have flux densities less than 100 G. This implies that hard microflares have underlying photospheric magnetic fields that are 5 to 10 times stronger than standard microflares. In addition, for the hard microflares with the classic two-footpoints morphology, the absolute value of the mean LoS magnetic field density at the footpoint rooted within the sunspot ranges from 600 to 1800 G, whereas the outer footpoint measures from 10 to 200 G. These values align with the magnetic flux densities of two case studies reported in Saqri et al. (2024). For the vector magnetic field density, we obtain 1500 to 2500 G for the footpoint rooted within the sunspot, while for the outer footpoint from 100 to 400 G (see Appendix B). This means that the magnetic flux density at the footpoint directly rooted within the sunspot can be about 10 times stronger than the outer footpoint.
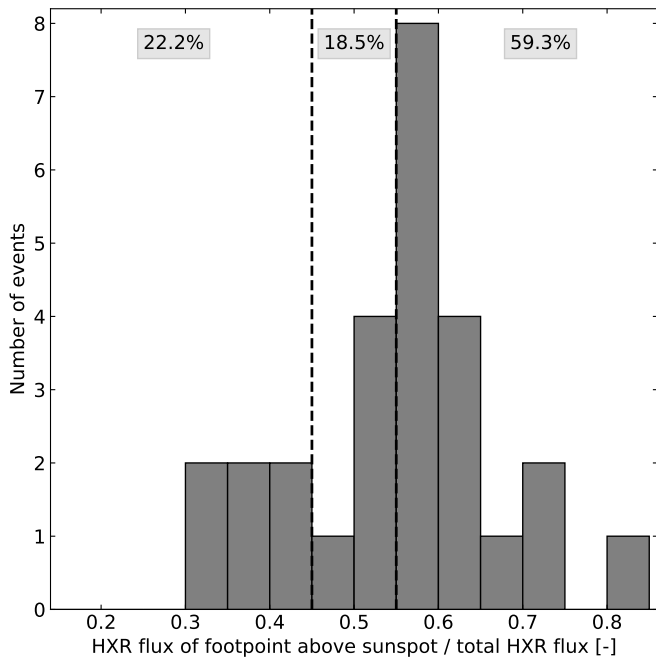
Fig. 7. For the events with two HXR footpoints, this figure shows the histogram of the HXR flux coming from the footpoint above the sunspot relative to the total flux of the two HXR sources. Values above 0.5 on the horizontal axis mean that the flux is higher in the footpoint directly rooted within the sunspot, and vice versa for values below 0.5. By taking into account the error on the flux estimation, events with values between 0.45 and 0.55 (interval defined by the vertical dashed lines) are considered to have similar HXR fluxes in the footpoints. Of all the events with two footpoints, 59.3% have a stronger HXR flux in the footpoint rooted directly within the sunspot, 18.5% have similar fluxes, and 22.2% have a stronger HXR flux in the footpoint outside the sunspot.

Interestingly, Tschernitz et al. (2018) does not report field densities larger than 800 G, even though they considered flares up to GOES class X27. This is on one hand related to the different analysis. Tschernitz et al. (2018) consider the full flare maps (over the overall flare duration) whereas here we only consider the pixels at the flare peak time. On the other hand, there is also an effect that hard microflares are anchored at photospheric field concentrations that are stronger than for regular flares. It is also important to note that flares have larger spatially extended ribbons compared to microflares. Therefore, averaging the field density over the ribbon area might result in a weaker field if the ribbons are spatially extended. However, this does not fail to highlight the strikingly intense magnetic flux densities observed in hard microflares, as it is also directly evidenced by their location inside the sunspots.

4. Discussions

4.1. How frequently do hard microflares occur?

In this subsection, we address the question of how frequently hard microflares occur on the Sun.

The most suitable dataset for estimating the occurrence frequency of hard microflares is the one by Hannah et al. (2008a), which includes thousands of RHESSI microflare events. According to that sample, about 1.5% of the events fall into the hard microflare regime, defined simply as microflares (GOES class below C2, see Appendix A) with an electron spectral index lower than 5. However, the events in Hannah et al. (2008a) were de-
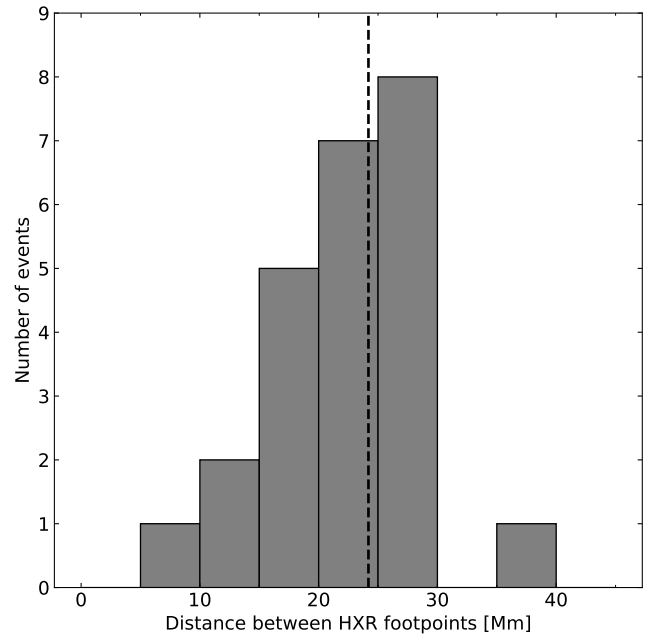

Fig. 8. For the events with two HXR footpoints, we show the distribution of their distance. The vertical dashed line represents the median distance, which corresponds to approximately 24 Mm.

tected at the peak of the thermal emission, which means that the nonthermal signal might have already significantly decreased. Therefore, this 1.5% is an underestimation. Since around half of our events have a different peak time in thermal and nonthermal emission, this means that about 3% of the events fall into the hard microflare regime, as estimated from Hannah et al. (2008a).

As outlined in Appendix A, we detected 74 events (39 of which observed from Earth) over a little more than 2 years of continuous STIX observations. Given that STIX observed about 20'000 flares in the same period, the number of hard microflares detected is underestimated, as 3% of 20'000 is 600. This underestimation is likely due to the combination between the method used in this paper together with the flare list on the STIX website (Xiao et al. 2023), which the latter is optimized for operational purposes and not science. An algorithm that relies on time profiles in the first step, rather than a pre-defined list, would be most effective for detecting all hard microflares.

4.2. Hard microflares in recent literature

While this paper introduces the term "hard microflares" for the first time, it is important to note that such events have been observed in the past already, particularly with instruments like RHESSI (e.g., Hannah et al. 2008b). In this subsection, we summarize the key findings from recent literature on these events.

In their study of 27 flares, as recorded by Konus-Wind and various microwave observatories, Lysenko et al. (2018) analyzed the relationship between HXRs and microwaves. Similar to hard microflares, they found that these events are weaker, shorter, and harder in the X-ray domain compared to standard flares. In the microwave domain, the events are shorter and harder, but not weaker. Furthermore, in the microwave domain, these events often demonstrated a significantly higher peak frequency than standard flares. This high peak frequency implies strong magnetic field, which aligns with our findings, because hard microflares originate in sunspots, which are regions of strong mag-
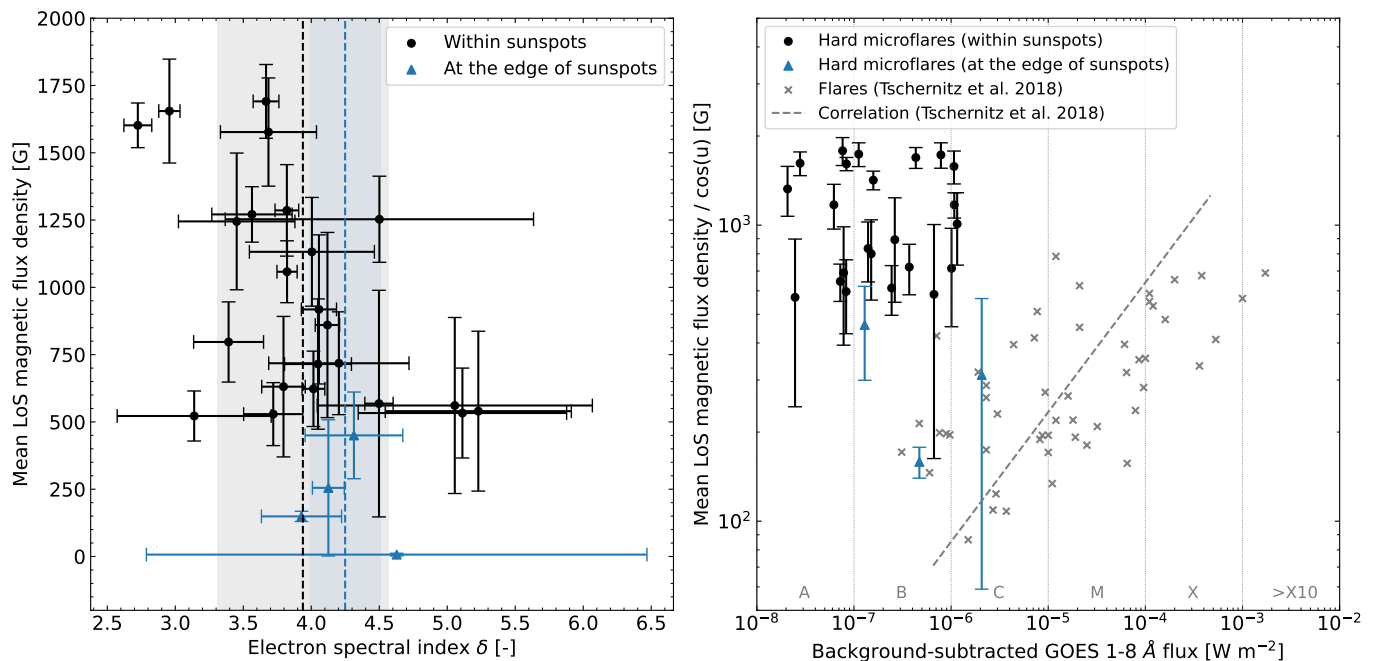
Fig. 9. Analysis of the photospheric line-of-sight (LoS) magnetic flux density of the flare footpoint located within or at the edge of the sunspot. (*Left*) Absolute value of the mean LoS magnetic flux density as a function of the electron spectral index. Black dots represent events with the footpoint within the sunspot, while blue triangles represent those at the edge of the sunspot. Vertical lines indicate the mean electron spectral indices, with the shaded areas representing its standard deviation. (*Right*) Absolute value of the mean LoS magnetic flux density against the background-subtracted GOES 1-8 Å SXR flux. The gray crosses and the dashed gray correlation curve are derived from Tschernitz et al. (2018, Figure 9). To be consistent with Tschernitz et al. (2018), in this plot we multiplied the mean LoS magnetic flux density by $1/\cos(u)$, with u the angular distance from disk center of the flare location.

netic fields. Consequently, this suggests that the events analyzed by Lysenko et al. (2018), termed as "cold" flares[3], are essentially hard microflares (see Fig. 6).

Lysenko et al. (2018) report that the strong magnetic field inferred from microwaves suggests a lower altitude of the radio source, as the magnetic field decreases with altitude. This is an indication of a shorter flaring loop or lower lying. Our findings suggests that the strong magnetic fields inferred from microwaves could be mainly due to the presence of the sunspot rather than the source-height. Although we find that approximately 54% of the events (which could be approximated with a single loop geometry) tend to exhibit a relatively flat loop (i.e., low-lying), roughly 33% of the events are well approximated by a semi-circle geometry, indicating they are not necessarily low-lying. In addition, the estimated loop-heights agree with that of standard microflares (Christe et al. 2011). Therefore, the presence of the strong magnetic field due to the sunspot seems to be more important. However, the strong magnetic field inferred from microwaves can derive from a combination of both, the low-laying sources combined with the strong magnetic field of the sunspots.

Let us now discuss the energy partitioning in the HXR observations of flares, which means how the total energy released during flares is distributed among different processes, such as thermal and nonthermal emission. Warmuth & Mann (2020) found, after comparing results from various studies, that the thermal-nonthermal energy partition changes with flare strength.

In weak flares, there appears to be a lack of energetic electrons, while in strong flares, the nonthermal energy injected is enough to account for the thermal component. However, Awasthi et al. (2024), after analyzing several microflares that occurred in September 2021, were able to deduce the ratio between the HXR fluence (the nonthermal emission integrated over time) and the SXR flux, which is primarily thermal emission. This ratio allowed them to identify nonthermal rich flares (events with a high value of this ratio), as shown in Fig. 6. These high ratio values suggest that the energy partitioning of these events differs from the standard trend reported by Warmuth & Mann (2020). The reason for this is not clear yet, but Awasthi et al. (2024) suggest that the plasma density in the coronal loops may play a crucial role in the thermal-nonthermal energy partition.

4.3. Hard HXR spectra, limited thermal response and strong magnetic fields

In the following, we address two questions that are not necessarily related. The first concerns the relationship between the hard particle spectra and the limited thermal response, specifically the chromospheric evaporation. The second question is why some small flares produce such hard electron spectra.

In response to the first question, it is important to note the two distinct types of evaporation: explosive (e.g., Milligan et al. 2006a) and gentle (e.g., Milligan et al. 2006b). These types differ in the speed at which the heated chromospheric plasma expands into the corona. Studies have found that this speed significantly depends on the energy flux density of the beam reaching the chromospheric plasma (e.g., Fisher et al. 1985). Simulations conducted by Reep et al. (2015) using the HYDRAD code (Brad-

---

[3] The origin of this term is due to the very low thermal response relative to nonthermal energy of accelerated particles in these events. However, the low thermal emission is not necessarily due to low temperature, but it can also be due to low emission measure at high temperature.

shaw & Cargill 2013) indicated that lower energy electrons are more efficient at heating the atmosphere (and consequently triggering evaporation) than higher energy electrons, especially in the case of gentle evaporation. For the explosive evaporation, instead, a weaker beam flux of low-energy electron is sufficient. So, why do such events have a limited thermal response then? A potential explanation could involve the pre-flare plasma density in the loop (e.g., Awasthi et al. 2024), which might stop some low-energy electrons in the corona from reaching the chromosphere. Combined with a very flat spectrum that does not generate enough low-energy electrons to trigger significant evaporation, this could explain the limited thermal response. However, to properly answer this question, a detailed analysis of the plasma conditions of the flare loop and a spectroscopic analysis of the evaporation are needed.

For the second question, we explore the reason why such small flares can produce hard electron spectra. Our key observational finding is that at least one of the footpoints is directly rooted in the sunspot. This suggests that the strength of the magnetic field is at the origin of the harder spectra of the accelerated electrons. However, how does this compare with various particle acceleration mechanisms reported in the literature, such as DC electric field acceleration (e.g., Holman 1985; Drake et al. 2006), stochastic acceleration (e.g., Stix 1992), and shock acceleration (e.g., Ellison & Ramaty 1985)? To address these questions in more details, we have to delve into the different models of particle acceleration and investigate the primary properties that result in hard spectra, and check whether there is a direct relationship with field strength. This intriguing question will be the focus of a future study.

4.4. Asymmetric HXR footpoints

There is another interesting aspect of hard microflares, which is the asymmetric HXR emission coming from the flare footpoints, in the case of the two-footpoints morphology.

One of the reasons for the asymmetric HXR footpoints reported in the literature is the magnetic mirroring effect (e.g., Sakao 1994; Sakao et al. 1996; Aschwanden et al. 1999). Accelerated electrons that spirals in the direction of increasing field strength (from the loop-top downwards) encounter an opposing force, due to the Lorentz force, which may persist until its parallel velocity to the field changes sign and reflects (e.g., Benz 2002, p. 30). Hence, electrons can get trapped between mirror points, which prevents them from advancing into areas of stronger magnetic fields. The stronger the magnetic field, the higher the mirror point. The higher the mirror point, the lower the density and the less likely electrons have collisions and emit HXR bremsstrahlung. As sunspots are areas of stronger magnetic field, by assuming that the density model on both sides of the simple magnetic loop is similar, the HXR flux from the footpoint in the sunspot should be lower. However, our key finding is that approximately 78% of hard microflares, which exhibited two HXR footpoints, have similar or even stronger flux from the footpoint rooted within the sunspot, which is inconsistent with the magnetic mirroring scenario, as in sunspots the magnetic field is much stronger relative to the surrounding regions.

This inconsistency with the magnetic mirroring could have different origins. The first could be associated with the asymmetry of the reconnection point where electron acceleration happens, potentially closer to the brighter footpoint (e.g., Goff et al. 2004; Falewicz & Siarkowski 2007).

The second reason is related to the asymmetric variation in plasma density along the loop (e.g., Falewicz & Siarkowski

2007). In such a case, a higher HXR flux is expected at the footpoint associated with the flank of the loop with a lower density. This increases the chance for accelerated electrons to lose their energy in the chromosphere and subsequently emit HXRs from the footpoint, whereas on the other side they lose some of the energy already in the corona. In this context, it is important to investigate the density in the active region at chromospheric and coronal altitudes directly above the sunspot with respect to the surrounding areas. This is because hard microflares have one footpoint rooted in the sunspot and another outside, somewhere in the active region. However, Tripathi et al. (2008) showed that, for the active region they investigated, the density in the corona directly above the sunspot is lower compared to the surrounding area (refer to Fig. 3 of their paper). This point should also be verified in the context of hard microflares. If it were not for the strong magnetic field in the sunspot, this condition would allow electrons to deposit most of their energy (at chromospheric altitudes) at the footpoint associated with the sunspot.

As previously mentioned, the mirroring effect can play a role here. It is important to note that this effect depends on the angle distribution of the accelerated electrons, hence the ratio $v/v_\perp^{top}$, where v represents the velocity of the electron, and $v_\perp^{top}$ is its perpendicular component at the top of the loop (e.g., Benz 2002), assuming that the reconnection point is at the top of the loop. The lower the $v_\perp^{top}$, the higher the field strength that can be accessed by electrons without being mirrored. This ratio defines the pitch angle α_{top} such as

$$\alpha_{top} = \arcsin\left(\frac{v_\perp^{top}}{v}\right). \tag{1}$$

Therefore, if the electron distribution is beamed, implying a narrow pitch angle distribution, electrons can penetrate the chromospheric layers, despite the strong magnetic field associated with the sunspot.

To determine if beaming is contributing to the asymmetry and the penetration of accelerated electrons in such a strong magnetic field, one can conduct stereoscopic X-ray observations of hard microflares. Solar Orbiter/STIX provides a unique viewpoint beyond the Sun-Earth line for this purpose. As demonstrated in Jeffrey et al. (2024), this allows us to evaluate the HXR directivity and investigate the pitch angle distribution of the accelerated electron beam.

4.5. Extension to regular flares

We discuss here the relationship between the electron spectral index and the strength of the magnetic field in the context of regular flares.

In this context, important results are already reported in the literature and it is a combination between two different types of studies. One one hand, in this work we show how the correlation curve by Warmuth & Mann (2016a) aligns well with the independent statistical studies by Battaglia et al. (2005) and Hannah et al. (2008a). This implies that the intensity of the flare, on the large scale of flare intensities from A to X GOES classes, is related to the efficiency of high-energy electron acceleration. In other words, a harder spectrum is associated with more intense flares, and this applies to both flares and microflares. On the other hand, Tschernitz et al. (2018) show that the more intense events correlate with stronger magnetic fields. Thus, these results suggest that a stronger magnetic field implies a harder spectrum.

This aligns with the observation that hard microflares are associated with stronger magnetic fields (i.e., rooted in sunspots) compared to standard (and softer) microflares. These findings highlight the universality of the results.

5. Conclusions and outlook

In this study, we analyzed 39 hard microflares. These events have relatively low thermal emission but a notably hard spectrum at higher energies, which means that they are very efficient in accelerating high-energy electrons. Our key findings from this statistical analysis are reported in the following.

- Hard microflares have one of the footpoints directly rooted within the sunspot, which suggests that the strength of the magnetic field is at the origin of the hard spectra observed in HXRs.
- For the events with the classic two-footpoints morphology, the absolute value of the mean LoS magnetic field density at the footpoint rooted within the sunspot ranges from 600 to 1800 G, whereas the outer footpoint measures from 10 to 200 G. For the vector magnetic field density, we obtain 1500 to 2500 G for the footpoint rooted within the sunspot, while for the outer footpoint from 100 to 400 G. This means that the magnetic flux density at the footpoint directly rooted within the sunspot can be about 10 times stronger than the outer footpoint.
- Despite the large difference of the magnetic field at the flare footpoints, approximately 78% of hard microflares, which exhibited two HXR footpoints, have similar or even stronger HXR flux from the footpoint rooted within the sunspot.
- The median footpoint separation, as measured by means of HXR observations, is approximately 24 Mm. This is consistent with events of similar GOES classes.
- About 74% of the events could be approximated by a simple loop geometry, demonstrating that hard microflares typically have a relatively simple morphology. Out of these events, around 54% exhibit a flat flare loop geometry, while roughly 33% of the events are well approximated by a semi-circle. The rest showed a high degree of tilting. Therefore, the loop-height is estimated to range between 6 and 12 Mm.

Hard microflares, due to their nature, offer excellent case studies for exploring electron acceleration in flares and the thermal plasma response to nonthermal electron input. Consequently, we believe that future studies should focus on addressing three primary scientific questions: Why do hard microflares exhibit a limited thermal response? What acceleration mechanism enables these small flares to generate such a hard spectrum? What is the primary factor causing the asymmetry of the HXR footpoint fluxes in these events? By addressing these questions through the study of hard microflares, we can gain a better understanding of the acceleration process and the thermal response in flares.

References

Antonucci, E., Gabriel, A. H., & Dennis, B. R. 1984, ApJ, 287, 917
Aschwanden, M. J. 2004, Physics of the Solar Corona. An Introduction
Aschwanden, M. J., Fletcher, L., Sakao, T., Kosugi, T., & Hudson, H. 1999, ApJ, 517, 977
Awasthi, A. K., Mrozek, T., Kołomański, S., et al. 2024, ApJ, 964, 142
Barnes, W., Cheung, M., Bobra, M., et al. 2020, The Journal of Open Source Software, 5, 2801
Battaglia, A. F., Saqri, J., Massa, P., et al. 2021, A&A, 656, A4
Battaglia, A. F., Wang, W., Saqri, J., et al. 2023, A&A, 670, A56
Battaglia, M., Grigis, P. C., & Benz, A. O. 2005, A&A, 439, 737
Benz, A. 2002, Plasma Astrophysics, second edition, Vol. 279
Benz, A. O. 2017, Living Reviews in Solar Physics, 14, 2
Bradshaw, S. J. & Cargill, P. J. 2013, ApJ, 770, 12
Christe, S., Krucker, S., & Saint-Hilaire, P. 2011, Sol. Phys., 270, 493
Del Zanna, G. & Young, P. R. 2020, Atoms, 8, 46
Dere, K. P., Landi, E., Mason, H. E., Monsignori Fossi, B. C., & Young, P. R. 1997, A&AS, 125, 149
Drake, J. F., Swisdak, M., Che, H., & Shay, M. A. 2006, Nature, 443, 553
Ellison, D. C. & Ramaty, R. 1985, ApJ, 298, 400
Falewicz, R. & Siarkowski, M. 2007, A&A, 461, 285
Fisher, G. H., Canfield, R. C., & McClymont, A. N. 1985, ApJ, 289, 414
Fletcher, L., Dennis, B. R., Hudson, H. S., et al. 2011, Space Sci. Rev., 159, 19
Freeland, S. L. & Handy, B. N. 1998, Sol. Phys., 182, 497
Goff, C. P., Matthews, S. A., van Driel-Gesztelyi, L., & Harra, L. K. 2004, A&A, 423, 363
Hannah, I. G., Christe, S., Krucker, S., et al. 2008a, ApJ, 677, 704
Hannah, I. G., Hudson, H. S., Battaglia, M., et al. 2011, Space Sci. Rev., 159, 263
Hannah, I. G., Krucker, S., Hudson, H. S., Christe, S., & Lin, R. P. 2008b, A&A, 481, L45
Hirayama, T. 1974, Sol. Phys., 34, 323
Hoeksema, J. T., Liu, Y., Hayashi, K., et al. 2014, Sol. Phys., 289, 3483
Högbom, J. A. 1974, A&AS, 15, 417
Holman, G. D. 1985, ApJ, 293, 584
Hudson, H. & Ryan, J. 1995, ARA&A, 33, 239
Inglis, A. R. & Christe, S. 2014, ApJ, 789, 116
Ishikawa, S.-n., Krucker, S., Ohno, M., & Lin, R. P. 2013, ApJ, 765, 143
Jeffrey, N. L. S., Krucker, S., Stores, M., et al. 2024, ApJ, 964, 145
Kleint, L., Heinzel, P., Judge, P., & Krucker, S. 2016, ApJ, 816, 88
Krucker, S., Hurford, G. J., Grimm, O., et al. 2020, A&A, 642, A15
Lemen, J. R., Title, A. M., Akin, D. J., et al. 2012, Sol. Phys., 275, 17
Lysenko, A. L., Altyntsev, A. T., Meshalkina, N. S., Zhdanov, D., & Fleishman, G. D. 2018, ApJ, 856, 111
Maurya, R. A., Vemareddy, P., & Ambastha, A. 2012, ApJ, 747, 134
Milligan, R. O., Gallagher, P. T., Mathioudakis, M., et al. 2006a, ApJ, 638, L117
Milligan, R. O., Gallagher, P. T., Mathioudakis, M., & Keenan, F. P. 2006b, ApJ, 642, L169
Müller, D., St. Cyr, O. C., Zouganelis, I., et al. 2020, A&A, 642, A1
Neupert, W. M. 1968, ApJ, 153, L59
Pesnell, W. D., Thompson, B. J., & Chamberlin, P. C. 2012, Sol. Phys., 275, 3
Reep, J. W., Bradshaw, S. J., & Alexander, D. 2015, ApJ, 808, 177
Saint-Hilaire, P., Krucker, S., & Lin, R. P. 2008, Sol. Phys., 250, 53
Sakao, T. 1994, PhD thesis, -
Sakao, T., Kosugi, T., Masuda, S., et al. 1996, Advances in Space Research, 17, 67
Saqri, J., Veronig, A. M., Battaglia, A. F., et al. 2024, A&A, 683, A41
Scherrer, P. H., Schou, J., Bush, R. I., et al. 2012, Sol. Phys., 275, 207
Schwartz, R. A., Csillaghy, A., Tolbert, A. K., et al. 2002, Sol. Phys., 210, 165
Stix, T. H. 1992, Waves in plasmas
SunPy Community, Barnes, W. T., Bobra, M. G., et al. 2020, ApJ, 890, 68
Tripathi, D., Mason, H. E., Young, P. R., & Del Zanna, G. 2008, A&A, 481, L53
Tschernitz, J., Veronig, A. M., Thalmann, J. K., Hinterreiter, J., & Pötzi, W. 2018, ApJ, 853, 41
Veronig, A., Vršnak, B., Dennis, B. R., et al. 2002, A&A, 392, 699
Volpara, A., Massa, P., Perracchione, E., et al. 2022, A&A, 668, A145
Warmuth, A. & Mann, G. 2016a, A&A, 588, A115
Warmuth, A. & Mann, G. 2016b, A&A, 588, A116
Warmuth, A. & Mann, G. 2020, A&A, 644, A172
Xiao, H., Maloney, S., Krucker, S., et al. 2023, A&A, 673, A142

Appendix A: Automatic hard microflare selection

Appendix A.1: Description of the methodology

The selection process for the hard microflares considered in this paper is detailed in the following. The complete list of the 39 selected events is provided in Tab. A.1.

STIX is the suitable instrument for detecting and studying hard microflares, as one of its key advantages is its constant non-solar background over the duration of the flare (e.g., Battaglia et al. 2021), a result of its deep space environment. Unlike X-ray detectors on Earth-orbiting missions, which are affected by photons produced by the interaction of high-energy particles from Earth's radiation belts and polar regions with the spacecraft, the STIX detectors maintain a stable non-solar background. Furthermore, since it orbits the Sun and is always pointing towards it, STIX doesn't have "nights," allowing for continuous observations. This uninterrupted observation and steady background make STIX ideal for detecting and analyzing relatively small events, such as microflares.

Among the events considered in this paper, Fig. 1 presents the quicklook time profiles of four examples of hard microflares of different GOES classes, from A2 to C1 (background subtracted). The peculiar behavior of these events is noteworthy, with all energy channels above 10 keV increasing impulsively around the nonthermal peak time (highlighted by the vertical black dashed line). In fact, in general, nonthermal emission is expected to be seen above 10 keV in microflares.

Our primary interest is in the spectral shape of the STIX flares at the nonthermal peak, which corresponds to the time when the bulk of accelerated electrons is injected into the chromosphere, producing higher energy photons. Therefore, the first step is to determine the nonthermal peak time of all flares observed by STIX. We achieved this by starting with the STIX flare list available on the STIX data center (Xiao et al. 2023) and we then identified the nonthermal peak by detecting peaks at the most energetic channels where the signal is above the background. In our approach, we adopted a simplistic method where we only accounted for a single peak per flare, even in events where multiple peaks are present. We chose the peak with more counts in the most energetic channel, which for microflares corresponds to the hardest peak. As hard microflares typically have just one peak with a hard spectrum, this approach is well justified for sorting out such events.

Once the nonthermal peak time of all flares is obtained, we can get the background-subtracted quicklook counts for all energy channels. To account for the varying distance of Solar Orbiter from the Sun, these peak counts are scaled to 1 AU. As previously noted, if microflares exhibit nonthermal emission, it typically occurs above approximately 10 keV (Hannah et al. 2008a, 2011). Hence, in the top panel of Fig. A.1, we plot the 10-15 keV quicklook background-subtracted counts against the 4-10 keV quicklook background-subtracted counts. As expected, a clear correlation between the two channels is evident. We also notice the increased sensitivity of STIX when Solar Orbiter is closer to the Sun. In order to select microflares, we only considered events with less than 1000 background-subtracted quicklook counts scaled at 1 AU in the 4-10 keV channel, which correspond to events of GOES X-ray flux lower than 2×10^{-6} W m^{-2} (Xiao et al. 2023), therefore lower than GOES C2 class.

For microflares, assuming an isothermal model and an additional nonthermal component fitting the higher energy part of the spectrum (see Fig. 2), the vertical distribution of points in Fig. A.1 reflects the spectral index of the nonthermal spectrum. As demonstrated by the four examples in the upper part of the cloud, the harder the spectrum, the higher the counts in the 10-15 keV channel. On the other hand, lower counts in the 10-15 keV channel, as demonstrated by the SOL2021-06-30 07:10 example, tend to show soft spectra or even the absence of nonthermal emission. Consequently, hard microflares tend to cluster around the upper part of the cloud of points.

Having observed the clustering of hard microflares in the scatter plot of Fig. A.1, we now need a way for their selection. In order to do this, we calculate the ratio between the background-subtracted quicklook counts of 10-15 and 4-10 keV and plot it against the date, as illustrated in the bottom panel of Fig. A.1. It is striking how hard microflares clearly stand out. By setting an arbitrary threshold value of 0.6, we can differentiate hard microflares from the standard ones. Using this value, we identified a total of 74 hard microflares between January 2021 and April 2023, with 34 being jointly observed from Earth. To the list of selected events, additional 5 events have been manually added to the list as from the STIX quicklook time profiles were clearly standing out. These five events, which range from October to December 2023, all fulfill the criteria previously described, namely less than 1000 background-subtracted STIX quicklook counts scaled at 1 AU in the 4-10 keV channel, observable from Earth, and the background-subtracted quicklook counts of 10-15 exceeding 0.6 times the 4-10 keV counts.

Appendix A.2: Influence of the selection threshold

This subsection explores the impact of the arbitrary threshold used to select hard microflares.

Apart from the criterion of being observable from Earth, which reduced potential candidates by about half, the events were chosen if the ratio between the background-subtracted quicklook counts of 10-15 and 4-10 keV exceeded 0.6. The selection of this value is arbitrary, and it significantly influences the number and nature of the selected events. With a 0.6 value, about 80% of the events are rooted within sunspots, and the rest are located at the edge of sunspots. However, Fig. 9 and Fig. B.1 reveal a trend for the hardest flares to be located in regions of stronger magnetic field densities, hence within sunspots. The weaker and softer ones are then located at the edge of sunspots. This suggests that if we would have chosen a higher threshold value (above 0.6), we might have selected only events rooted within sunspots[4]. This is because the higher the ratio, the harder the spectrum.

Appendix B: Vector magnetic field density at the hard microflare footpoints

Because in sunspots the umbral and penumbral magnetic fields have a very different inclination, in this appendix we present the analysis of the vector magnetic field density at the photosphere, as opposed to the line-of-sight magnetic field density extracted from the magnetograms. This is achieved by analyzing the total field strength, from the hmi.B_720s data series (Hoeksema et al. 2014), at the same footpoint locations as described in Sect. 2.2.

In Fig. B.1, the vector magnetic field flux density is shown against the electron spectral index δ. The trend is similar and the results are consistent with what we reported in Fig. 9. However,

---

[4] The statement concerning whether all standard microflares are not rooted in sunspots has not been tested yet. This verification can be done by considering lower selection thresholds and observing if one only detects events rooted outside sunspots. This is currently the subject of an ongoing separate study.

Table A.1. List of all the hard microflares analyzed in this paper.

Event #	Flare peak time[a]	SO Coord.[b]		Earth Coord.[c]		GOES[d]	δ^e [-]	AR[f]	Category[g]	Flare loop[h]
		x ['']	y ['']	x ['']	y ['']					
1	22-Sep-2021 10:11:48	100	-830	-422	-555	B1	3.7 ± 0.2	AR12871	within	complex
2	22-Sep-2021 18:52:16	140	-800	-375	-560	A6	5.1 ± 0.8	AR12871	within	flat
3	22-Sep-2021 20:12:36	150	-800	-400	-530	B3	3.8 ± 0.2	AR12871	within	semi-circle
4	4-Oct-2021 06:50:46	-1170	370	-950	210	A1	4.2 ± 0.3	AR12882	within	flat
5	4-Oct-2021 08:37:02	-1170	350	-900	217	A2	4.8 ± 0.5	AR12882	within	flat
6	4-Oct-2021 09:36:58	-1160	350	-892	223	A1	3.3 ± 0.3	AR12882	within	flat
7	9-Oct-2021 00:23:04	10	340	-240	150	<A1	4.0 ± 0.5	AR12882	within	tilted
8	11-Oct-2021 19:23:50	780	330	345	165	A2	3.0 ± 0.1	AR12882	within	complex
9	3-Feb-2022 02:14:11	1070	300	752	320	A3	3.6 ± 1.6	AR12936	within	flat
10	3-Feb-2022 05:53:59	1070	300	775	315	A2	3.4 ± 0.3	AR12936	within	flat
11	3-Feb-2022 12:45:24	1100	340	811	334	B1	4.3 ± 1.6	AR12936	edge	flat
12	3-Feb-2022 20:41:59	1110	290	820	350	B3	4.9 ± 0.3	AR12936	within	-
13	30-Mar-2022 08:38:43	-2740	670	230	355	B1	4.1 ± 0.1	AR12976	within	semi-circle
14	8-May-2022 04:20:42	-1190	-260	805	-185	A4	3.1 ± 0.3	AR13003	within	complex
15	10-Nov-2022 17:14:35	620	140	25	150	A4	3.7 ± 0.1	AR13141	within	unclear
16	12-Nov-2022 04:32:50	980	160	320	160	A4	3.9 ± 0.3	AR13141	edge	complex
17	13-Nov-2022 10:25:27	1230	250	576	192	A2	5.1 ± 0.7	AR13141	within	semi-circle
18	24-Nov-2022 06:22:24	650	-450	250	-268	B1	4.8 ± 0.3	AR13151	edge	complex
19	8-Dec-2022 07:37:56	530	-410	200	-255	A5	4.3 ± 0.4	AR13153	edge	complex
20	19-Dec-2022 08:17:20	-510	230	-745	325	A5	3.3 ± 0.5	AR13169	edge	semi-circle
21	22-Dec-2022 14:52:04	240	230	-84	330	A3	2.7 ± 0.1	AR13169	within	unclear
22	23-Dec-2022 04:34:29	370	220	38	345	A8	3.7 ± 0.4	AR13169	within	tilted
23	15-Jan-2023 23:45:12	-410	240	-730	345	A5	4.4 ± 0.3	AR13192	within	complex
24	16-Jan-2023 00:29:40	-300	-350	-660	-216	A5	4.5 ± 1.1	AR13190	within	complex
25	16-Jan-2023 03:44:12	-280	-350	-637	-210	B1	3.8 ± 0.1	AR13190	within	flat
26	21-Feb-2023 02:06:15	300	550	-261	545	A6	4.6 ± 1.8	AR13229	edge	tilted
27	28-Feb-2023 13:49:12	1000	610	380	535	A7	4.2 ± 0.5	AR13234	within	semi-circle
28	11-Mar-2023 07:52:00	-1820	-230	325	-280	<A1	3.5 ± 0.4	AR13245	within	flat
29	11-Mar-2023 14:32:57	1120	-600	390	-325	A7	4.1 ± 0.1	AR13245	within	complex
30	11-Mar-2023 21:14:43	1180	-500	422	-260	B1	3.6 ± 0.3	AR13245	within	semi-circle
31	11-Mar-2023 22:43:00	1180	-570	424	-290	A8	4.0 ± 0.2	AR13245	within	flat
32	12-Mar-2023 06:07:13	1230	-570	475	-300	B2	4.0 ± 0.1	AR13245	within	semi-circle
33	12-Mar-2023 17:46:01	1310	-600	551	-310	A2	3.1 ± 0.6	AR13245	within	flat
34	3-Apr-2023 18:29:29	-560	-950	171	-310	A1	5.1 ± 1.0	AR13270	within	semi-circle
35	18-Oct-2023 20:57:01	2250	400	321	121	A4	5.3 ± 0.3	AR13465	edge	unclear
36	30-Oct-2023 03:48:10	250	-730	-215	-346	B2	4.5 ± 0.1	AR13474	within	flat
37	23-Nov-2023 07:12:15	-450	170	-525	230	C1	4.1 ± 0.1	AR13492	edge	complex
38	30-Nov-2023 15:42:09	650	-510	400	-338	B4	3.8 ± 0.1	AR13500	within	unclear
39	26-Dec-2023 23:50:53	900	-400	749	-337	B1	4.6 ± 0.5	AR13529	within	flat

[a]: STIX nonthermal peak time corrected for the light travel time difference.
[b]: Aspect corrected helioprojective coordinates in the Solar Orbiter reference frame. No additional shift is considered.
[c]: Helioprojective coordinates in the Solar Dynamics Observatory reference frame.
[d]: Pre-flare subtracted GOES class determined at the nonthermal peak time.
[e]: Electron spectral index.
[f]: NOAA active region number.
[g]: If (at least) one of the footpoints is within or at the edge of the sunspot. No distinction is made between umbra and penumbra.
[h]: Flare loop geometry determined from the AIA 131 Å maps. There is not AIA coverage for event 12 (footpoint location determined with GONG).
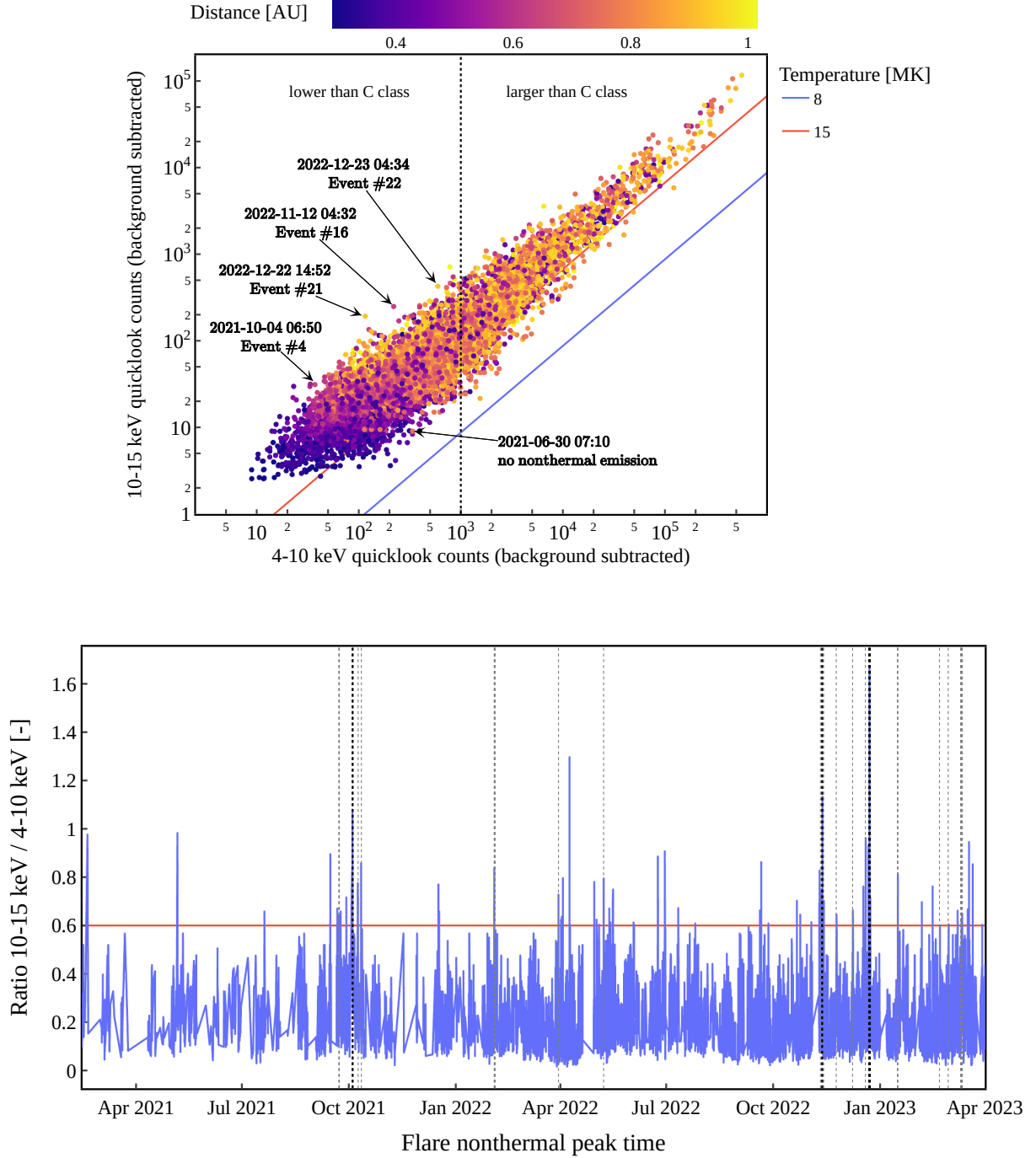
Fig. A.1. Summary of the event selection of the hard microflares. (*Top*) Scatter plot of the 10-15 keV STIX quicklook background-subtracted counts against the 4-10 keV quicklook background-subtracted counts at the nonthermal peak, for all flares from February 2021 to April 2023. All counts have been scaled to 1 AU. The color code refers to the Solar Orbiter distance to the Sun at the time of the observation. The blue and red lines show the expected STIX quicklook counts in the case of flares with a purely isothermal component of 8 MK and 15 MK temperature, respectively. In the scatter plot, we highlighted the same events as shown in Figs. 1 and 2. We can clearly observe how hard microflares cluster on the upper part of the cloud. (*Bottom*) Ratio between the 10-15 keV to 4-10 keV quicklook curves as function of date, from February 2021 to April 2023. The hard microflares clearly stand out as spikes. The horizontal red line indicates the chosen threshold of 0.6 to identify hard microflares. The vertical dashed gray lines mark the events selected for this statistical analysis and the vertical dashed black lines highlight the same four hard microflares as in the scatter plot.

some interesting differences are worth to be highlighted. First of all, the overall field strength is more elevated in this case, because we are considering the total field strength and not only the line-of-sight component. Secondly, we note a larger sample of harder events, with respect to Fig. 9, to be associated with stronger magnetic field strengths (> 2000 G). This reflects the true nature of the strong magnetic fields in sunspots, regardless
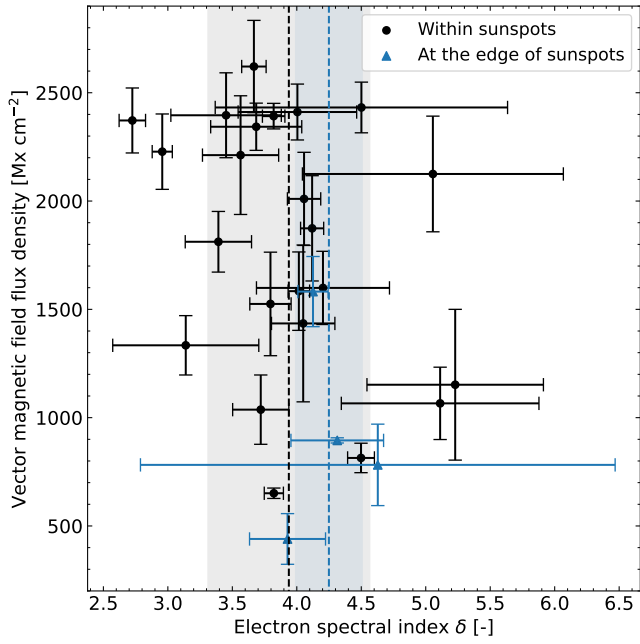
Fig. B.1. Analysis of the vector magnetic field density of the flare foot-point located within or at the edge of the sunspot. This figure is similar to the left panel of Fig. 9, with the difference that here we consider vector magnetic field data. We note that $1\,\mathrm{Mx\,cm^{-2}} = 1\,\mathrm{G}$.

of the magnetic field orientation compared to the line-of-sight, as it is the case for the standard magnetograms.

In the case of the hard microflares with the classic two-footpoints morphology, the mean field strength at the footpoint rooted within the sunspot ranges from 1500 to 2500 G, whereas the outer footpoint measures from 100 to 400 G. This difference is consistent with the results obtained in the context of the standard magnetogram data, as the field strength at the footpoint rooted within the sunspot can be about 10 times stronger than that of the outer footpoint.